AIAA JOURNAL
Vol. 56, No. 2, February 2018

Aerodynamic Heating in Wall-Modeled Large-Eddy Simulation of High-Speed Flows

X. I. A. Yang* and J. Urzay†
Stanford University, Stanford, California 94305
S. Bose‡
Cascade Technologies Inc., Palo Alto, California 94303
and
P. Moin§
Stanford University, Stanford, California 94305

DOI: 10.2514/1.J056240

Aerospace vehicles flying at supersonic and hypersonic speeds are subject to increased wall heating rates caused by viscous friction with the gas environment. This extra heat is commonly referred to as convective aerodynamic heating. In wall-modeled large-eddy simulations, the near-wall region of the flow is not resolved by the computational grid. As a result, the effects of aerodynamic heating need to be modeled using a large-eddy simulation wall model. In this investigation, wall-modeled large-eddy simulations of turbulent high-speed flows are performed to address this issue. In particular, an equilibrium wall model is employed in high-speed turbulent Couette flows subject to different combinations of thermal boundary conditions and grid sizes as well as in transitional hypersonic boundary layers interacting with incident shock waves. Specifically, the wall-modeled large-eddy simulations of the Couette flow configuration demonstrate that the shear-stress and heat-flux predictions made by the wall model show only a small sensitivity to the grid resolution even in the most adverse case where aerodynamic heating prevails near the wall and generates a sharp temperature peak there. Additionally, the simulations indicate that the wall model predicts shear stresses and heat fluxes that are mostly proportional to the near-wall velocity in a manner that resembles an approximate power law. In the wall-modeled large-eddy simulation of hypersonic boundary-layer/shock-wave interaction, the model is tested against direct numerical simulations and experiments. It is shown to correctly capture aerodynamic heating and the overall heat transfer rate around the shock-impingement zone, despite the fact that the adverse pressure gradients in that region may involve nonequilibrium effects.

Nomenclature

A	=	wall-damping constant
a	=	speed of sound
B_q	=	wall heat-transfer coefficient
C_f	=	skin-friction coefficient
c_p	=	specific heat at constant pressure
h_{wm}	=	large-eddy simulation/wall-model matching location from the wall
L	=	length scale
M	=	Mach number
N	=	number of grid cells
P	=	static pressure
Pr	=	Prandtl number
q	=	heat flux
Re_δ	=	bulk Reynolds number
Re_τ	=	friction Reynolds number
R_g	=	gas constant
S	=	Sutherland constant
St	=	Stanton number
T	=	static temperature
t_f	=	flow-through time
U	=	velocity
u_τ	=	friction velocity
x	=	streamwise direction
y	=	wall-normal direction
z	=	spanwise direction
Δ	=	grid spacing
δ	=	half-channel height
δ^*	=	displacement thickness
κ	=	von Kármán constant
μ	=	viscosity
ρ	=	density
τ	=	shear stress

Subscripts

b	=	bottom-wall quantity
t	=	top-wall quantity
w	=	wall quantity
wm	=	wall-model quantity
$\parallel$	=	wall-parallel quantity
$+$	=	normalization by wall units
∞	=	freestream quantity

Received 24 April 2017; revision received 29 August 2017; accepted for publication 25 October 2017; published online 28 November 2017.

*Postdoctoral Researcher, Center for Turbulence Research.
†Senior Research Engineer, Center for Turbulence Research.
‡Chief Technology Officer.
§Professor, Center for Turbulence Research.

I. Introduction

NEAR-WALL turbulence modeling is a relevant discipline for engineering problems that involve wall-bounded turbulent flows and heat transfer. In particular, examples where wall heat transfer plays an important role include inlets and combustors in air-breathing hypersonic propulsion systems [1], fuselages of high-speed aerospace vehicles during reentry or hypersonic cruise flight [2], and the first rows of turbine blades immediately downstream of the combustor in jet engines [3]. Because of the associated complexity and computational cost of high-fidelity simulations including direct numerical simulations (DNSs) and wall-resolved large-eddy simulations (LES), most of the early near-wall treatments are based on empirical correlations calibrated a priori for specific types of flows [4,5] and wall functions in Reynolds-averaged Navier–Stokes simulations [6,7]. Besides the aforementioned methods, wall-modeled large-eddy simulation (WMLES) is becoming

viable as an attractive high-fidelity alternative to DNS in industrial design [8]. In WMLES, the bulk of the flow is resolved, and only the near-wall turbulence is modeled.

Most of the earlier work on WMLES has been focused on addressing the momentum transfer near the wall (e.g., see reviews in [9,10]), with focus being made mostly on low-speed flows such as incompressible channel flows [11,12], atmospheric boundary layers [13,14], urban boundary layers [15,16], and low-speed transitional boundary layers [17]. Wall heat-transfer modeling in high-speed flows, on the other hand, has received much less attention in comparison with wall shear-stress modeling. The reason perhaps is that the Reynolds analogy and the Monin–Obukhov similarity theory, according to which the wall heat transfer is slaved to the wall shear stress, have so far worked fairly well in low-speed flows [18,19]. However, at high speeds, such simplification cannot be exploited due to the disjoining effect of the aerodynamic heating near the wall, which makes modeling the thermal field an additional challenge that has to be undertaken in these types of flows.

High-speed wall-bounded flows involve a number of additional physical processes that complicate LES wall modeling. Predictions of the velocity field in principle tend to rely on predictions of thermal fields, and vice versa, particularly in high-Mach-number regimes, where significant density variations occur near the wall that couple the momentum and thermal-energy conservation equations. Additionally, high-speed flows tend to involve impingement of shock waves on boundary layers along with aerodynamic heating. The former aspect has been discussed, for example, in [20,21] within the context of WMLES of fully developed turbulent supersonic boundary layers interacting with shock waves above adiabatic walls. In practical applications, such as hypersonic flows around aerospace vehicles or internal flows in supersonic combustors, however, heat transfer to walls plays an important role, and WMLES strategies have demonstrated promise in capturing complex phenomena there [22]. At high Mach numbers, the heat-transfer effect induced by both convective and radiative aerodynamic heating is significant near the wall. Correspondingly, coarse grids typically used in LES may not be able to capture this effect because they do not resolve this region, and an appropriate LES wall model is required.

This investigation focuses on the role of convective aerodynamic heating in wall heat-transfer modeling in WMLES of turbulent flows in the supersonic and hypersonic velocity ranges (Mach 2–6). Additional effects such as the radiative transfer connected with nonequilibrium thermochemical processes, sometimes enabled by the high flow temperatures near the fuselage of high-speed aerospace vehicles, are not considered in this work. The wall model under consideration is an equilibrium one (see [23] and Sec. II for details). Although the equilibrium wall model has been used previously for computing high-speed turbulent flows [20,22], the present study provides a first systematic analysis of grid convergence and model performance in different flow configurations. In particular, the capability of the model in capturing the wall heat-transfer rates is tested in high-speed Couette flows and transitional boundary layers interacting with incident shock waves. The results show that the model performs remarkably well even in cases where the intense, near-wall aerodynamic heating is not resolved by the LES grid.

The remainder of this paper is organized as follows. The model formulation is summarized in Sec. II for later use throughout the paper. The model performance is first tested in Sec. III for high-speed Couette flows and later in Sec. IV for the case of an oblique shock wave impinging on a transitional hypersonic boundary layer. Last, conclusions and comments on future work are provided in Sec. V.

II. Equilibrium Wall Model

The equilibrium wall model integrates the momentum and total-energy conservation equations

$$\frac{d}{dy}\left[(\mu+\mu_{t,\mathrm{wm}})\frac{du_\parallel}{dy}\right]=0 \tag{1}$$

$$\frac{d}{dy}\left[(\mu+\mu_{t,\mathrm{wm}})u_\parallel\frac{du_\parallel}{dy}+c_p\left(\frac{\mu}{Pr}+\frac{\mu_{t,\mathrm{wm}}}{Pr_{t,\mathrm{wm}}}\right)\frac{dT}{dy}\right]=0 \tag{2}$$

within a layer spanning from the wall $y=0$ to a matching location $y=h_{\mathrm{wm}}$, where appropriate boundary conditions are applied, as explained later. In this formulation, y is the wall-normal coordinate; $u_\parallel$ is the total wall-parallel velocity including both the streamwise and spanwise components; T is the static temperature; c_p is the specific heat at constant pressure; $Pr=0.7$ is the molecular Prandtl number; μ is the molecular dynamic viscosity; and the subscript "wm" indicates unclosed quantities modeled in the wall model.

The molecular viscosity μ is a function of the temperature, with the particular dependence being provided in Secs. III and IV for each of the two problems treated here. Additionally, the eddy viscosity $\mu_{t,\mathrm{wm}}$ is specified according to the mixing-length model

$$\mu_{t,\mathrm{wm}}=\kappa\rho y\sqrt{\frac{\tau_w}{\rho}}D \tag{3}$$

where $\kappa=0.4$ is the von Kármán constant, ρ is the density, and τ_w is the local wall shear stress. The van Driest damping function D is given by

$$D=\left[1-\exp\left(-\frac{y^+}{A^+}\right)\right]^2 \tag{4}$$

where the superscript "+" indicates lengths normalized by the instantaneous local wall unit $\delta_\nu=\nu_w/u_\tau$, with ν_w and u_τ being the wall kinematic viscosity and friction velocity, respectively. In Eq. (4), $A^+=17$ is a model constant indicating the dimensionless height above the wall where the molecular and eddy viscosities become of the same order of magnitude.

Density and temperature are related through the equation of state:

$$P=\rho R_g T \tag{5}$$

where R_g is the gas constant, and P is the static pressure; the latter is considered to be a constant across the wall-modeled region that matches with the LES pressure at the LES/wall-model interface. Last, $Pr_{t,\mathrm{wm}}=0.9$ is the eddy Prandtl number. Note that the model does not include a wall-normal velocity component, a streamwise pressure gradient, nor time variations of momentum and energy, and it does not account for total-energy transfer by pressure work.

Equations (1) and (2) along with Eqs. (3–5) are numerically integrated on a one-dimensional grid $0\le y\le h_{\mathrm{wm}}$ bounded by the wall at $y=0$ and by a matching location at $y=h_{\mathrm{wm}}$ where the wall-model solution matches with the LES solution on the coarse grid. Following Kawai and Larsson [23], the matching location is set to $h_{\mathrm{wm}}=2.5\Delta_y$, where Δ_y is the WMLES grid spacing in the wall-normal direction. This matching height corresponds to the third LES grid point (cell center) from the wall. The boundary conditions for the wall model at the wall $y=0$ are

$$u_\parallel=U_w,\quad T=T_w\ \text{(isothermal wall) or}\ dT/dy=0\ \text{(adiabatic wall)} \tag{6}$$

where U_w and T_w are the wall velocity (for moving surfaces) and wall temperature, respectively. For isothermal walls, the wall temperature is kept uniform along the wall and constant in time. The corresponding boundary conditions at the matching location $y=h_{\mathrm{wm}}$ are

$$u_\parallel=\tilde{U}_\parallel,\qquad T=\tilde{T},\qquad P=\overline{P} \tag{7}$$

where $\tilde{U}_\parallel$, $\tilde{T}$, and $\overline{P}$ are the resolved LES values of wall-parallel velocity, static temperature, and static pressure. The former includes the streamwise and spanwise components as appropriate depending on the local direction of the resolved LES flow at the matching location. In this notation, the tilde and overline operators indicate Favre and Reynolds filtering, respectively. The equilibrium wall model provides the necessary boundary conditions for the integration of the outer LES

equations. Specifically, the first LES cell from the wall is fed with the wall shear stress $\tau_w = \mu du_\parallel/dy|_{y=0}$ and the wall heat flux $q_w = (\mu c_p/Pr)dT/dy|_{y=0}$ from the solution to the wall-model problem [Eqs. (1–7)].

A. Remarks on the Equilibrium Wall-Modeled Energy Equation

In anticipation of the results presented later, it is convenient to highlight two different aspects of the energy equation [Eq. (2)]. The first one relates to the representation of the aerodynamic heating in the equilibrium wall model. Upon integrating Eq. (1) once, the first term on the left-hand side of Eq. (2) can be easily rewritten as a molecular dissipation given by $\tau_w(du_\parallel/dy)$, which corresponds to the subgrid-scale (SGS) aerodynamic heating and becomes important at sufficiently high Mach numbers.

To estimate the relative importance of the aerodynamic heating in Eq. (2), consider a freestream at velocity U_∞ and temperature T_∞ flowing along a colder stationary wall at temperature T_w. The two terms involving the temperature gradient in Eq. (2) represent the molecular heat conduction $(c_p\mu/Pr)dT/dy$ and the turbulent heat transport $(c_p\mu_{\text{wm}}/Pr_{t,\text{wm}})dT/dy$. The former prevails over the latter close to the wall where $y^+ \ll (A^+)^{2/3}$; note that requiring $\mu_{\text{wm}}/\mu \sim \kappa y^+[1-\exp(-y^+/A^+)]^2 \sim \kappa y^+(y^+/A^+)^2 \ll 1$ leads directly to $y^+ \ll (A^+)^{2/3}$. The opposite occurs relatively far away from the wall, when $y^+ \gg A^+$, where the ratio of molecular to eddy viscosities is small, $\mu/\mu_{\text{wm}} \sim 1/(\kappa y^+) \ll 1$. Focusing first on the region where molecular effects prevail, the aerodynamic heating scales as $\tau_w u_\tau/\delta_\nu$, whereas the heat conduction becomes of order $c_p\mu_w T_\tau/\delta_\nu^2$, where δ_ν is the viscous length scale, and $T_\tau \sim q_w/(\rho_w c_p u_\tau)$ is a friction temperature [24] that characterizes temperature variation across the viscous sublayer and can be further simplified by using the Reynolds analogy $q_w \sim \tau_w c_p(T_\infty - T_w)/U_\infty$ (assuming that the Reynolds analogy still applies). As a result, in this region, when the condition

$$(\gamma-1)\left(\frac{T_\infty}{T_\infty - T_w}\right)M_\infty^2 C_f^{1/2} = O(1) \tag{8}$$

is satisfied, the aerodynamic heating becomes of the same order as the molecular heat conduction, $\tau_w u_\tau/\delta_\nu \sim c_p\mu_w T_\tau/\delta_\nu^2$. In Eq. (8), γ is the adiabatic coefficient, C_f is the skin friction coefficient, and M_∞ is the freestream Mach number. Conversely, in the region where turbulent heat transport prevails, the assumption of approximate logarithmic laws for velocity and temperature, $du_\parallel/dy \sim u_\tau/(\kappa y)$ and $dT/dy \sim T_\tau/(\kappa_T y)$, suggests the scaling $\tau_w u_\tau/(\kappa y)$ for the aerodynamic heating and $c_p\mu_{\text{wm}}T_\tau/(Pr_{t,\text{wm}}\kappa_T y^2)$ for the divergence of the turbulent heat flux, with the latter being further simplified by assuming $Pr_{t,\text{wm}} \sim \kappa/\kappa_T$ [25] and using the asymptotic expression $\mu_{\text{wm}} \sim \kappa\rho_\infty y u_\tau$ emerging from the eddy-viscosity model [Eq. (3)] at $y^+/A^+ \gg 1$. Consequently, in this region, the aerodynamic heating becomes of the same order as the turbulent heat transport when the condition

$$(\gamma-1)\left(\frac{T_\infty}{T_\infty - T_w}\right)\left(\frac{\rho_w}{\rho_\infty}\right)\frac{M_\infty^2}{\kappa} C_f^{1/2} = O(1) \tag{9}$$

is satisfied. Because the temperature and density variations are typically of order unity, both conditions [Eq. (8) and (9)] approximately lead to $M_\infty^2 C_f^{1/2} = O(1)$, indicating that aerodynamic heating becomes important throughout the entire wall-modeled layer when $M_\infty \sim C_f^{-1/4}$, which translates into Mach numbers of order 3–5 when $C_f \sim$ 0.001–0.005 as in the simulations detailed later (up to premultiplying factors of order unity). When such high Mach numbers are met, the resulting aeroheated region is typically not resolved by WMLES grids, in which the spacing in the wall-normal direction scales with the local boundary layer height. As described in Secs. III and IV, in some WMLES cases, the aerodynamic heating modeled as described previously leads to nonmonotonic SGS temperature profiles within the wall-modeled region by which heat is transferred both to the wall and to the bulk flow.

The second aspect worth highlighting is related to the coupling of the SGS aerodynamic heating with the resolved LES field. Under the equilibrium assumption, the bracketed quantities in Eqs. (1) and (2) are constant across the wall-modeled layer. These conserved quantities correspond to the sum of the viscous and turbulent shear stresses [in Eq. (1)] and to the sum of aerodynamic heating, molecular heat conduction, and turbulent heat transport [in Eq. (2)]. Of particular interest for interpreting the performance of the equilibrium wall model is the latter invariance. To see this, consider a wall at rest, or equivalently a reference frame moving with the wall, in such a way that $U_w = 0$ for illustration. Specifically, the first integral of Eq. (2) evaluated at the matching location yields

$$q_w = \left(u_\parallel \tau_w + c_p\frac{\mu_{t,\text{wm}}}{Pr_{t,\text{wm}}}\frac{\partial T}{\partial y}\right)_{y=h_{\text{wm}}} \tag{10}$$

where the molecular heat conduction has been neglected on the right-hand side because $\mu/\mu_{\text{wm}} = O(\delta_\nu/h_{\text{wm}}) \ll 1$ there. Equation (10) states that the wall heat flux is the sum of the aerodynamic heating and the turbulent heat transport at the matching location, with each represented by the first and second terms on the right-hand side, respectively. This conservation constraint, for instance, indicates that, in adiabatic flows ($q_w = 0$), the slope of the temperature at the edge of the wall-modeled layer is not necessarily zero in high-speed conditions described previously where aerodynamic heating becomes important because that extra heat must be evacuated to the bulk flow. Note, however, that the right-hand side of Eq. (10) cannot be exactly equated to the equivalent expression written in terms of the LES quantities $\tilde{U}$ and $\tilde{T}$ because such constraint is not strictly imposed at the matching location. In an asymptotic sense, and if the LES conservation equations effectively reduced to Eq. (2) close to the wall, expression (10) could be approximated as

$$q_w \approx \left(\tilde{U}_\parallel \tau_w + c_p\frac{\mu_{t,\text{LES}}}{Pr_{t,\text{LES}}}\frac{\partial \tilde{T}}{\partial y}\right)_{y/\delta\to 0, y^+\gg 1} \tag{11}$$

where $\mu_{t,\text{LES}}$ and $Pr_{t,\text{LES}}$ are the LES eddy viscosity and turbulent Prandtl number, respectively, δ is a large scale (e.g., a boundary-layer thickness or half-channel height), and the bracketed quantities are evaluated sufficiently close to the wall but outside the viscous sublayer. The results described in Sec. III suggest that Eq. (11) is qualitatively correct, in that the action of the aerodynamic heating $\tilde{U}_\parallel$ close to the wall regulates the slope of the resolved LES temperature field, to the extent, for instance, that $\partial\tilde{T}/\partial y|_{y/\delta\to 0, y^+\gg 1} \neq 0$ in adiabatic conditions, where $q_w = 0$.

B. Code Numerics

The performance of this equilibrium wall model in capturing the wall heat-transfer rates is examined in Sec. III in high-speed turbulent Couette flows and in Sec. IV in a shock/transitional-boundary-layer interaction problem. The numerical code used in this study is the unstructured, finite volume compressible solver CharLES [20,26], which has been extensively used and validated for wall-bounded flow calculations (see for example [20,22,27,28]). The code solves the Favre-filtered compressible Navier–Stokes equations for the conserved flow quantities of mass, momentum, and total energy. The eddy viscosity is modeled using the Vreman model [29] for the results presented in Sec. III, whereas the dynamic Smagorinsky (DS) model [30] is used for those in Sec. IV. Among those two, the choice of SGS model did not lead to significant differences in the Couette flow configuration, but the local character of the DS model led to improved predictions in the problem of the shock interaction with a transitional boundary layer. A fourth-order central scheme is used for flux reconstruction in regions away from shocks, which are detected using a Ducros shock sensor [31,32] with a typical threshold of 0.02. Near shocks, an essentially nonoscillatory scheme is used. A third-order explicit Runge–Kutta scheme is used for time integration. Recent applications of this code in the context of WMLES can be found, for instance, in [33].

III. High-Speed Turbulent Couette Flows

A. Computational Set-up

Consider a turbulent flow between two parallel plates moving at the same speed U_w but in opposite directions, as sketched in Fig. 1. The top- and bottom-wall temperatures are denoted as $T_{w,t}$ and $T_{w,b}$, respectively. The subscripts b and t are used throughout this section to indicate quantities at the bottom and top walls. The computational domain has dimensions $L_x \times L_y \times L_z = 2\pi\delta \times 2\delta \times 2\pi\delta$ in the streamwise, wall-normal, and spanwise directions, respectively, where δ is the half-channel height. A structured Cartesian grid with uniform grid spacing in each direction is used. The grid spacings Δ_x, Δ_y, and Δ_z and the matching height h_{wm} are such that $\Delta_x/h_{\text{wm}} = \Delta_z/h_{\text{wm}} = 0.63$ and $\Delta_y/h_{\text{wm}} = 0.4$. The reader is referred to [34] for investigations of the effects of varying the ratio Δ_x/Δ_z. Periodic boundary conditions are imposed in the streamwise and spanwise directions. Statistics are averaged spatially in both x and z directions, and temporally for $\sim 100t_f$, where $t_f = L_x/U_w$ is the flow-through time, which, in these simulations, is of the same order as the large-scale eddy turnover time δ/u_τ.

The cases computed here are summarized in Tables 1–3. The wall Mach numbers range from $M_w \approx 1$ to 6 based on the local speed of sound, with grid sizes ranging from 55,000 to 8 million elements. Isothermal conditions with equal wall temperatures ($T_{w,b} = T_{w,t}$) are addressed in Sec. III.B, cases with unequal wall temperatures ($T_{w,b} \neq T_{w,t}$) are studied in Sec. III.C, and last adiabatic wall conditions ($q_{w,t} = 0$) are considered in Sec. III.D.

The results shown later focus on the performance of the equilibrium wall model under different grid resolutions and thermal boundary conditions. In particular, the analysis reports the dimensionless heat rate in the form of the parameter

$$B_q = q_w/(\rho_w c_p u_\tau T_w) \tag{12}$$

along with the skin friction

$$C_f = 2\tau_w/(\rho_w U_w^2) \tag{13}$$

and the friction Reynolds number

$$Re_\tau = \rho_w u_\tau \delta/\mu_w \tag{14}$$

In Eqs. (12–14), $q_w, \tau_w, \rho_w, \mu_w$, and T_w are averaged in time and in the spanwise and streamwise directions (note that the last three vary in space and time when adiabatic wall conditions are employed). The friction velocity is then computed as $u_\tau = \sqrt{\tau_w/\rho_w}$. Note that B_q, C_f, and Re_τ generally have different values on each wall, as prescribed by the evaluation of each parameter $q_w, \tau_w, \rho_w, \mu_w$, and T_w on either the upper or bottom wall, unless the boundary conditions are the same on both walls, in which case the differences are not significant in the statistically steady state.

The sound speed at the bottom wall ($a_{w,b} = \sqrt{\gamma R_g T_{w,b}}$), the bottom wall temperature $T_{w,b}$, the volume-averaged density ρ_m, and the half-channel height δ are the same in all the cases and are used for nondimensionalizing the results. Quantities with a superscript "+" are normalized with inner units corresponding to $\delta_\nu = \nu_w/u_\tau$ as the unit length and u_τ as the unit velocity. The molecular dynamic viscosity μ is made to vary with temperature according to the power law $\mu/\mu_{\text{ref}} = (T/T_{\text{ref}})^\sigma$, where $T_{\text{ref}} = T_{w,b}$ and $\mu_{\text{ref}} = \mu_{w,b}$ are the reference values of temperature and viscosity, respectively, and $\sigma = 0.7$ is the power exponent. The results presented next are focused on quantities that are conserved in WMLES, such as the mean values of velocity, temperature, wall shear stress, and wall heat transfer. Outer scales are employed for normalizing the wall-normal direction in the figures shown later because aerodynamic heating generally prevents logarithmic scaling of the mean velocity and temperature.

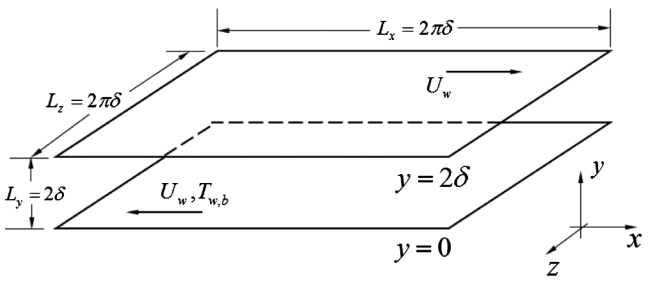

Fig. 1 Schematics of the computational setup for WMLES of high-speed turbulent Couette flows.

B. Isothermal Walls at the Same Wall Temperature

Six baseline cases, denoted as AX and BX in Table 1, are first described that are characterized by having upper and bottom walls at equal temperatures $T_{w,b} = T_{w,t}$. Cases beginning with the letters A and B correspond to $M_w = 3$ and $M_w = 6$, respectively, where $M_w = U_w/a_{w,b}$ is the Mach number. Note that M_w, B_q, C_f, and Re_τ are the same for both walls. The digit X is an index proportional to the grid size ($X = 1$ is the coarsest resolution and $X = 3$ is the finest one). The bulk Reynolds number, which is based on $\delta, U_w, \mu_{w,t}$, and ρ_m, is $Re_\delta = 3.0 \times 10^4$ for the Mach 6 cases and $Re_\delta = 1.5 \times 10^4$ for the Mach 3 cases.

All the cases with equal wall temperatures lead to monotonic temperature profiles near the wall. This can be observed in Fig. 2, which shows the profiles of mean velocity and temperature for the Mach 3 cases in Table 1. Because of the aerodynamic heating, the bulk temperature is higher than that at the wall. Specifically, the higher the Mach number is, the larger the bulk-to-wall temperature ratio is, which becomes 2.4 for the Mach 3 cases and 6.5 for the Mach 6 cases.

The mean velocity and temperature are fairly independent of the grid resolution for the grid sizes considered here. However, the LES solutions from the wall up to the third grid point on the LES grid appear to be grid-dependent, with the temperature profile from the coarse A1 grid falling consistently below that from the finer-grid calculations A2 and A3. This is similar to the observations made in [23] regarding WMLES of supersonic channels and boundary layers. There, grid-independent results were found only for values of h_{wm} above the third LES grid point from the wall. Despite these differences in the near-wall LES profiles, the wall quantities C_f, B_q, and Re_τ are mostly grid-independent for the two wall Mach numbers considered here, as shown in Table 1. Note that, although the sharp near-wall gradients in both profiles are poorly resolved in case A1 in comparison with A3, the subgrid profiles obtained from the wall model are similar for all grids, as shown in Fig. 2 where the wall-modeled profiles collapse near the wall. The convergence of the subgrid profiles and the absence of noticeable variations in C_f, B_q, and Re_τ indicate that the increasingly larger portions of unresolved velocity and temperature near the wall are correctly modeled by the equilibrium wall model. As a consequence, the wall heat fluxes and shear stresses become mostly independent of the grid size. The small differences detected in both C_f and B_q with grid refinement might be ascribed to the underperformance of the SGS model for the dissipation in Eq. (2) and a lack of statistical convergence, although these aspects have not been investigated in detail here. Similar conclusions are inferred from the BX cases (plots not shown here for brevity).

C. Isothermal Boundary Conditions with Different Wall Temperatures

The next two sets of cases, CX and DX, pertain to isothermal walls at different temperatures with $T_{w,t} = 9T_{w,b}$, as summarized in Table 2. The bottom-wall Mach number in both sets of cases is $M_{w,b} = 6$. As a result of the increase in the top wall temperature, the sound speed $a_{w,t} = \sqrt{\gamma R_g T_{w,t}}$ increases, and the top-wall Mach number decreases to $M_{w,t} = 2$. Cases CX and DX differ in their bulk Reynolds numbers, with $Re_\delta = 3.0 \times 10^4$ for CX and $Re_\delta = 1.2 \times 10^5$ for DX. Similar to the previous subsection, X is an index proportional to the grid resolution.

Because the flow is statistically stationary, the mean shear stress at the top wall balances that at the bottom wall. The differences between

Table 1 WMLES cases of high-speed turbulent Couette flows between two isothermal walls at the same temperature

Case	M_w	$N_x \times N_y \times N_z$	$\Delta_x^+ \times \Delta_y^+ \times \Delta_z^+ (\cdot 10^2)$	C_f	B_q	Re_τ
A1	3.0	$64 \times 32 \times 64$	$1.32 \times 0.842 \times 1.32$	0.00286	0.137	1.35×10^3
A2	3.0	$128 \times 64 \times 128$	$0.665 \times 0.424 \times 0.665$	0.00287	0.135	1.35×10^3
A3	3.0	$256 \times 128 \times 256$	$0.339 \times 0.216 \times 0.339$	0.00293	0.137	1.38×10^3
B1	6.0	$64 \times 32 \times 64$	$4.90 \times 3.12 \times 4.90$	0.00131	0.366	4.99×10^3
B2	6.0	$128 \times 64 \times 128$	$2.45 \times 1.56 \times 2.45$	0.00131	0.365	5.00×10^3
B3	6.0	$256 \times 128 \times 256$	$1.23 \times 0.782 \times 1.23$	0.00133	0.367	5.00×10^3

Table 2 WMLES cases for high-speed turbulent Couette flows between two isothermal walls at different temperatures ($T_{w,t} = 9T_{w,b}$)[a]

Case	M_w	$N_x \times N_y \times N_z$	$\Delta_x^+ \times \Delta_y^+ \times (\Delta_z^+ \cdot 10^2)$	C_f	B_q	Re_τ ($\times 10^3$)
C1	2.0	$48 \times 24 \times 48$	$0.513 \times 0.327 \times 0.513$	0.00686	0.0655	0.392
C1	6.0	$48 \times 24 \times 48$	$7.19 \times 4.58 \times 7.19$	0.000768	0.363	5.49
C2	2.0	$128 \times 64 \times 128$	$0.185 \times 0.118 \times 0.185$	0.00715	0.0665	0.377
C2	6.0	$128 \times 64 \times 128$	$2.59 \times 1.64 \times 2.59$	0.000795	0.369	5.27
D1	2.0	$48 \times 24 \times 48$	$1.80 \times 1.14 \times 1.80$	0.00481	0.0547	1.37
D1	6.0	$48 \times 24 \times 48$	$25.1 \times 16.0 \times 25.1$	0.000536	0.306	19.2
D2	2.0	$128 \times 64 \times 128$	$0.674 \times 0.430 \times 0.674$	0.00489	0.0549	1.37
D2	6.0	$128 \times 64 \times 128$	$9.46 \times 6.02 \times 9.45$	0.000546	0.307	19.2

[a]Values at the top and bottom walls are listed consecutively in each of the two rows for every case.

Table 3 WMLES cases for high-speed turbulent Couette flows between an upper adiabatic wall and a lower isothermal wall[a]

Case	M	$N_x \times N_y \times N_z$	$\Delta_x^+ \times \Delta_y^+ \times \Delta_z^+ (\times 10^2)$	C_f	B_q	Re_τ ($\times 10^3$)
E1	1.1	$64 \times 32 \times 64$	$0.171 \times 0.109 \times 0.171$	0.010049	0.0	0.17
E1	3.0	$64 \times 32 \times 64$	$1.83 \times 1.16 \times 1.83$	0.001419	0.1876	1.86
E2	1.1	$128 \times 64 \times 128$	$0.0905 \times 0.0577 \times 0.0905$	0.01094	0.0	0.18
E2	3.0	$128 \times 64 \times 128$	$0.974 \times 0.620 \times 0.974$	0.001525	0.194	1.98

[a]Values at the top and bottom walls are listed consecutively in each of the two rows for every case. The top-wall Mach number is based on the planar averaged speed of sound evaluated there.

the top- and bottom-wall skin-friction coefficients are due to the different densities on each wall. Although the bottom-wall shear stresses in cases CX are not very different from those in cases BX (i.e., 0.127 for CX and 0.154 for BX), the bottom-wall skin-friction coefficient is significantly smaller in the CX cases due to the additional factors participating in the normalization. Note, however, that the resulting heat-transfer fluxes at the bottom wall are not significantly different from those in the BX cases (i.e., 0.98 for CX and 0.91 for BX). Similarly, as the top-wall density decreases due to the increase in wall temperature, the viscous length $\mu_{w,t}/(\rho_{w,t}u_{\tau,t})$ increases. Correspondingly, the flow near the top wall is better numerically resolved than the flow near the bottom wall, which makes the grid resolution in the parallel directions near the top wall in case C2 comparable to a typical wall-resolved LES.

The increase in the top-wall temperature also has an important physical effect enabled by near-wall aerodynamic heating, in that it generates a near-wall peak in the temperature profiles in all cases, as shown in Fig. 3. As the top-wall temperature is increased, this peak moves increasingly closer to the top wall. If the top-wall temperature were increased to very high values, the peak temperature would be

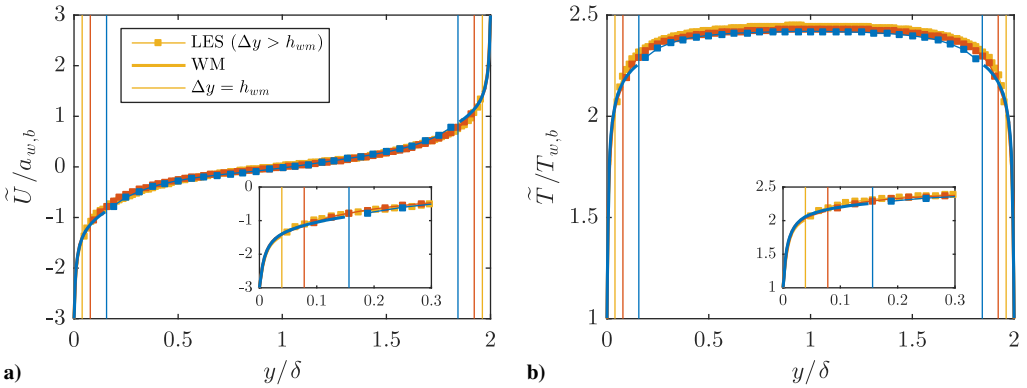

Fig. 2 a) Mean streamwise velocity and b) mean temperature profiles for the AX cases outlined in Table 1. In each case, the matching location $y = h_{\mathrm{wm}}$ is indicated using thin vertical lines, which move toward the wall as the grid is refined. The inset shows an amplified view of the profiles near the bottom wall. LES solutions within $h_{\mathrm{wm}} < y < 2\delta - h_{\mathrm{wm}}$ are shown using symbols (at grid points). SGS profiles computed from the equilibrium wall model (WM) in the wall-modeled regions $0 < y < h_{\mathrm{wm}}$ and $2\delta - h_{\mathrm{wm}} < y < 2\delta$ are shown using solid bold lines (two of the lines are indistinguishable from the third one). Colors indicate results computed on the finest grid (A3, yellow lines), coarsest grid (A1, blue lines), and intermediate grid (A2, orange lines).

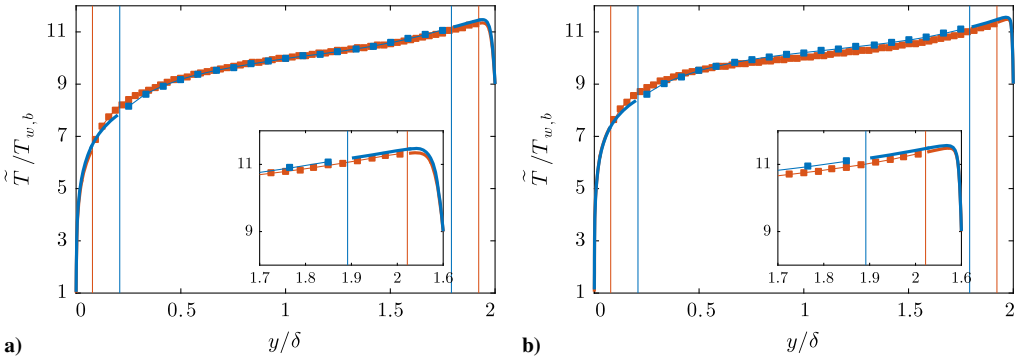

Fig. 3 Mean temperature for cases a) CX, and b) DX in Table 2. Refer to Fig. 2 for legends.

located there. At the intermediate top-wall temperature analyzed here, $T_{w,t} = 9T_{w,b}$, the peak temperature caused by aerodynamic heating sits near the top wall. Specifically, the peak temperature is partially resolved in cases C2 and D2 by the LES grid, whose resolution in both cases is high enough to warrant capturing this phenomenon. However, in cases C1 and D1, which are computed on coarser grids, the peak temperature ceases to be captured in the LES grid, as observed in Fig. 3. Despite this apparent shortfall, the heat-transfer coefficients B_q predicted by the equilibrium wall model in cases C1 and D1 are very similar to the ones obtained using the finer grids in cases C2 and D2, as indicated in Table 2. This indicates that aerodynamic heating has been correctly accounted for by the wall model in the computation of the near-wall temperature profile. Note, however, that the skin-friction coefficients for the CX cases increase by approximately 4% when the grid is refined by a factor of 2.5. This weak dependency of C_f on the grid resolution does not alter significantly the performance of the model regarding heat transfer rates, as shown in Table 2.

D. Mixed Isothermal/Adiabatic Boundary Conditions

The effect of adiabatic boundary conditions is addressed in cases EX in Table 3, which correspond to a bulk Reynolds number $Re_\delta = 1.5 \times 10^4$. In these cases, the bottom wall is isothermal, and the top one is adiabatic. The resulting profiles of temperature are shown in Fig. 4. Because the heat generated from aerodynamic heating near the top wall can only escape the computational domain through the bottom wall, the mean temperature peaks at the top wall with a temperature $T_{w,t} \approx 7T_{w,b}$. As a result, the flow near the top wall is better resolved than that near the bottom wall. The WMLES results show a small sensitivity to the grid resolution, with approximately a 6% difference being observed in the skin-friction and heat-transfer coefficients upon doubling the grid resolution in all three directions from case E1 to E2.

As discussed in Sec. II within the context of the energy equation [Eq. (2)] in the wall model, the temperature resolved on the LES grid does not necessarily have to arrive with zero slope at the adiabatic wall, particularly in high-speed flows where aerodynamic heating is important, as in the present configuration. Conversely, the LES temperature slope at the adiabatic wall increasingly departs from zero as the grid is coarsened, which finds justification in the fact that the aerodynamic heat generated in the near-wall region (computed by the equilibrium wall model) must be transferred into the bulk flow. The adiabatic boundary condition is strictly satisfied on the physical wall, in the form of a zero gradient of the temperature at $y = 0$ within the wall-modeled region. Therefore, the resulting wall heat-transfer rates reported in Table 3 become mostly insensitive to the grid resolution and to the presence or absence of adiabaticity in the resolved temperature field.

The results presented in the previous three subsections systematically illustrate the grid convergence and physical performance of the equilibrium wall model in high-speed flows for a number of different resolutions and wall boundary conditions. In particular, the grid convergence observed here indicates that, as the grid is refined, the LES conservation equations increasingly reproduce the results previously predicted by the wall model on coarser grids, thereby suggesting that the wall model captures some of the relevant physics associated with thermal coupling in high-speed wall-bounded turbulent flows. The remaining portion of this section addresses the nature of the predicted wall quantities and their dependence on the flow variables at the matching location.

E. Correlations of Wall Quantities with Velocities and Temperatures at the Matching Location

A question of some interest for LES modeling of wall-bounded flows is the relation between wall-based quantities such as the shear stress τ_w and the heat flux q_w as a function of the LES flow variables at the matching location, including the temperature $\tilde{T}$ and wall-parallel velocity $\tilde{U}_\parallel$. These two LES flow variables correspond to the upper boundary conditions of the wall model, as described in Sec. II.

In cases where both walls are isothermal and kept at the same temperature, as in case A2 in Table 1, the near-wall structure of the streamwise velocity $\tilde{U}$ and temperature $\tilde{T}$ at the matching location with the wall model are correlated with the corresponding wall-shear stress $\tau_{w,b}$ and wall heat flux $q_{w,b}$. This is shown in the in-plane

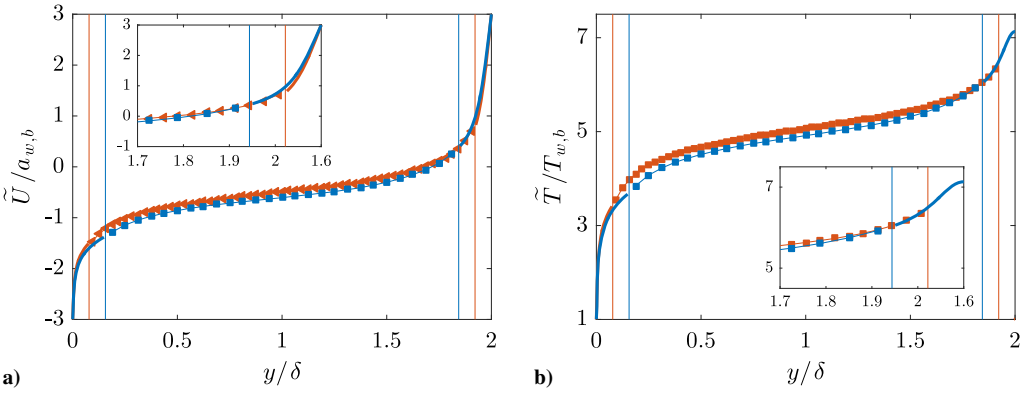

Fig. 4 a) Mean streamwise velocity and b) temperature for cases EX in Table 3. Refer to Fig. 2 for legends.

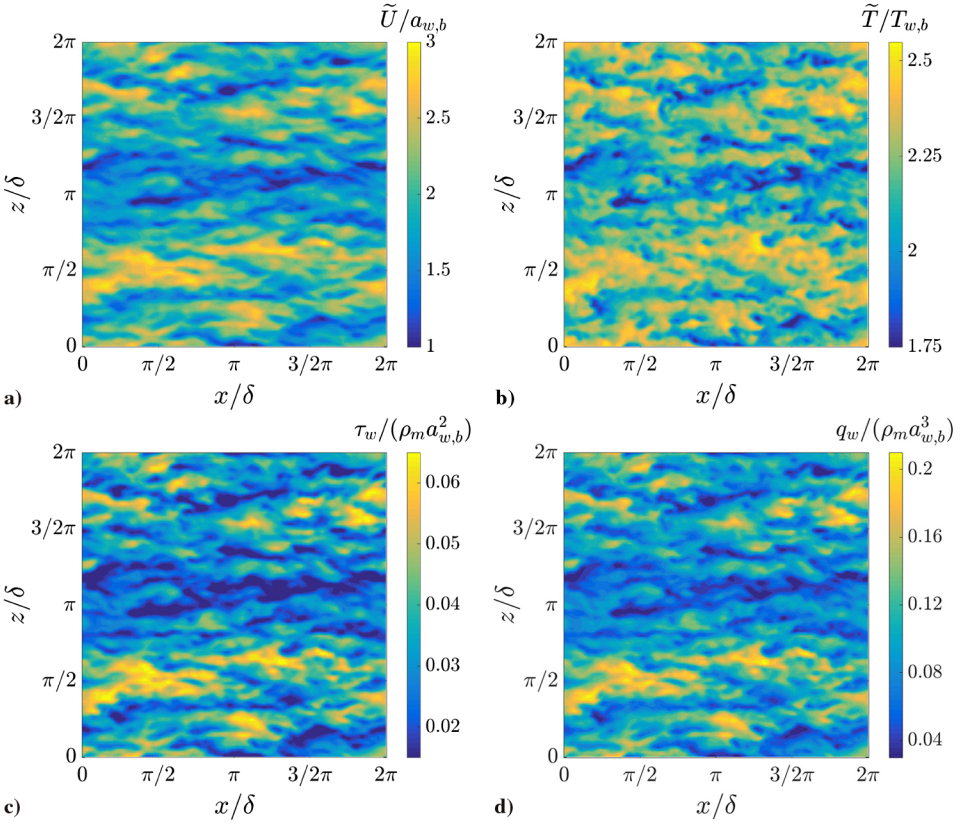

Fig. 5 Case A2 instantaneous isocontours of a) streamwise velocity, and b) temperature, both evaluated at the matching location with the wall model away from the bottom wall, along with c) bottom-wall shear stress, and d) bottom-wall heat flux. The flow goes from left to right. In these plots, the frame of reference moves at the bottom-wall speed $U_{w,b}$.

visualizations in Fig. 5 (cross-correlation coefficients $c_{\tilde{T},q_w} = 0.89$ and $c_{\tilde{U},\tau_w} = 0.97$; any phase lag between the wall quantities and the LES solutions at the matching location is absent in the current wall model formulation). Streaky structures can be discerned in all the contours. Similarly, in cases where the wall temperatures are different, as in case C2 in Table 2, the wall heat flux and shear stress are correlated with each other and with the near-wall structure of the streamwise velocity at the matching location, as observed in Fig. 6 (cross-correlation coefficients $c_{\tilde{U},q_{w,t}} = 0.93$ and $c_{\tilde{U},\tau_{w,t}} = 0.97$). However, the near-wall temperature is poorly correlated from the other three quantities, particularly with the wall heat transfer (cross-correlation coefficient $c_{\tilde{T},q_{w,t}} = 0.25$). This is in contrast with the equal-temperature case shown in Fig. 5, where both quantities are highly correlated, and it suggests that aerodynamic heating, rather than turbulent heat conduction, is here the dominant mechanism in modulating the temperature distribution at the matching location. Last, analogous in-plane contours provided in Fig. 7 for the mixed isothermal/adiabatic case E2 show that, at the adiabatic wall, the shear stress is correlated with the velocity and anticorrelated with temperature at the matching location (correlation coefficients $c_{\tilde{U},\tau_{w,t}} = 0.99$ and $c_{\tilde{T},\tau_{w,t}} = -0.87$), with the latter being explained by the monotonic decrease in temperature away from the wall.

The considerations given previously suggest that τ_w and q_w are correlated in all cases with the near-wall velocity, whereas such proportionality relation of τ_w and q_w with the near-wall temperature is not as discernible. This is shown in Fig. 8, where panels Figs. 8a and 8b suggest that a power-law scaling may exist between the shear stress, heat flux, and the near-wall velocity in all cases except for the mixed isothermal/adiabatic one, in which the relation appears to be more complex as revealed by the slight curvature of the scatter cloud. The scaling of the wall shear stress, however, is subject to a finite width vertical spread caused by the inherent dependence of this quantity on the near-wall temperature, as explained later.

In incompressible flows with constant viscosity, the solution to Eqs. (1) and (2) has the following characteristics. First, the near-wall velocity and wall shear stress are related as

$$\tilde{U}_\parallel = \tau_w \int_0^{h_{\mathrm{wm}}} F(y, \tau_w)\, \mathrm{d}y$$

in the reference frame moving with the wall velocity, where $F = 1/(\mu + \mu_{\mathrm{wm}})$ is a function that depends on y and τ_w, thereby rendering a nonlinear relation between $\tilde{U}_\parallel$ and τ_w with zero spread. Second, the near-wall temperature is given by

$$\tilde{T} - T_w = \int_0^{h_{\mathrm{wm}}} G(y, \tau_w, q_w)\, \mathrm{d}y$$

where $G = (q_w/c_p)(\mu/Pr + \mu_{\mathrm{wm}}/Pr_{t,\mathrm{wm}})^{-1}$ is a function that depends on y, τ_w, and q_w. If the molecular and turbulent Prandtl numbers are assumed to be unity, then F and G are simply related as $G = q_w F/c_p$, and the equilibrium wall model predicts the Reynolds analogy, $q_w = \tau_w c_p(\tilde{T} - T_w)/\tilde{U}_\parallel$. In addition, when the integration of the equilibrium wall-model equations is made indefinite in the wall-normal coordinate, the pointwise proportional relation $u_\parallel/\tau_w \sim (T - T_w)/(q_w/c_p)$ between the temperature and velocity profiles is obtained throughout the wall-modeled layer.

Conversely, in high-speed flows, the solution to Eqs. (1) and (2) is equivalent to simultaneously integrating

$$u_\parallel = \int_0^y \frac{\tau_w\, \mathrm{d}y}{\mu + \mu_{\mathrm{wm}}} \tag{15}$$

and

$$\int_0^y \frac{\tau_w^2\, \mathrm{d}y}{\mu + \mu_{\mathrm{wm}}} + c_p\left(\frac{\mu}{Pr} + \frac{\mu_{\mathrm{wm}}}{Pr_{t,\mathrm{wm}}}\right)\frac{dT}{dy} = q_w \tag{16}$$

subject to $u_\parallel = \tilde{U}_\parallel$ and $T = \tilde{T}$ at the matching location $y = h_{\mathrm{wm}}$. In particular, Eq. (15) indicates that the velocity field is additionally influenced by the local near-wall temperature through the viscosity coefficients, which necessarily leads to spreading in the τ_w versus $\tilde{U}_\parallel$

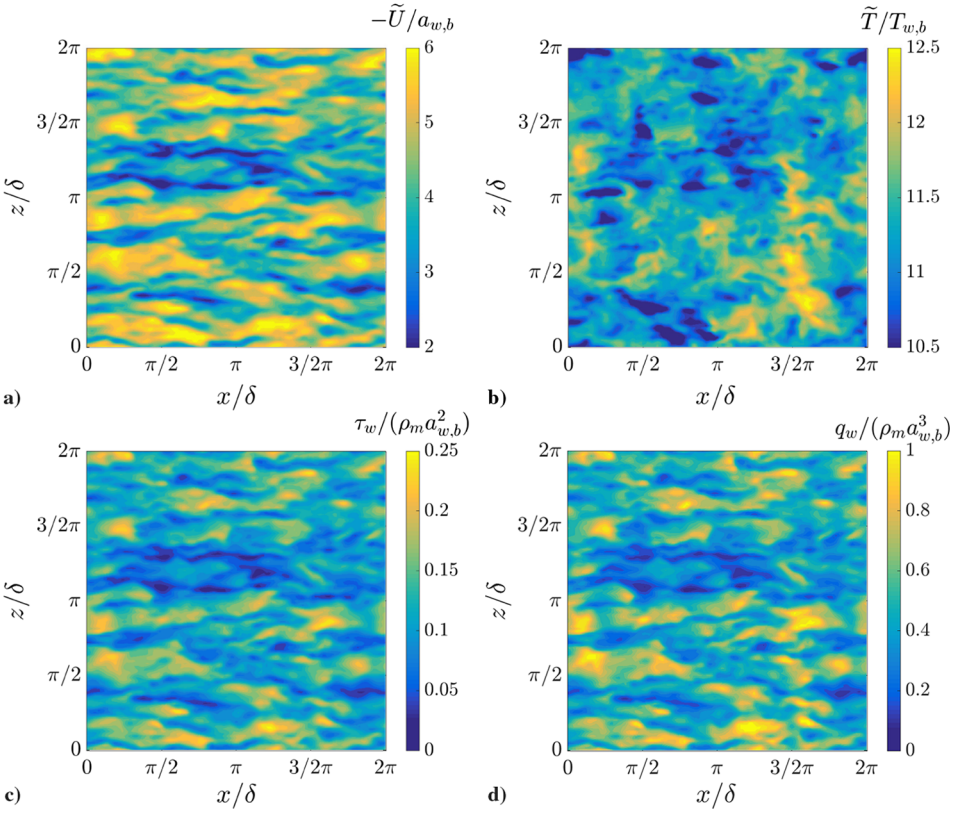

Fig. 6 Case C2 instantaneous isocontours of a) streamwise velocity, and b) temperature, both evaluated at the matching location with the wall model away from the top wall, along with c) top-wall shear stress and d) top-wall heat flux. The flow goes from left to right. In these plots, the frame of reference moves at the top-wall speed.

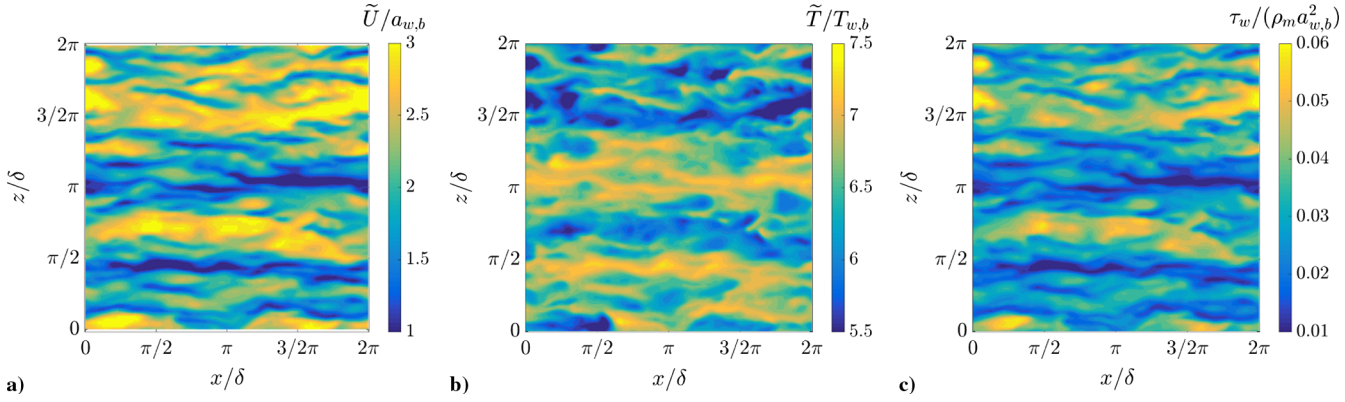

Fig. 7 Case E2 instantaneous isocontours of a) streamwise velocity, and b) temperature, both evaluated at the matching location with the wall model away from the top wall, along with c) top-wall shear stress. The flow goes from left to right. In these plots, the frame of reference moves at the top-wall speed.

plot. Similarly, Eq. (16) is an autonomous integrodifferential equation that only depends on temperature and contains two separate terms on the left-hand side that correspond to aerodynamic heating and heat transport, whose competition describes the relative importance of these two mechanisms in determining the wall heat flux q_w. When the aerodynamic heating term prevails in the near-wall region, as in case C2, the temperature dependence enters in q_w primarily through the viscosity coefficients, thereby leading to poor correlations of q_w and τ_w with the near-wall temperature, as observed in Figs. 8c and 8d. It is worth mentioning that although the temperature and velocity profiles cease to be proportional within the wall-modeled region when the aerodynamic heating is important, which suggests a breakdown of the classic Reynolds analogy, the shear stresses and heat fluxes remain mostly proportional, as observed in Fig. 8e.

IV. Shock-Wave Interaction with a Transitional Hypersonic Boundary Layer

In this section, the performance of the equilibrium wall model described in Sec. II is tested against DNS and experimental data in a Mach 6 transitional boundary layer interacting with an incident shock wave. The corresponding computational set-up is sketched in Fig. 9. The size of the computational domain is $L_x \times L_y \times L_z = 300 \times 25 \times 45$ in units of the displacement thickness $\delta_o^\star$ at the domain entrance. Two grid sizes are considered, namely $N_x \times N_y \times N_z = 256 \times 64 \times 72$ (~1 million cells) and $512 \times 64 \times 144$ (~4 million cells), which are denoted as WMLES1 and WMLES2 in what follows. The corresponding resolutions in viscous units on the fully turbulent region are $\Delta x^+ \times \Delta y^+ \times \Delta z^+ = 40 \times 16 \times 23$ and $20 \times 16 \times 11$, respectively. In terms of a large scale, such as the

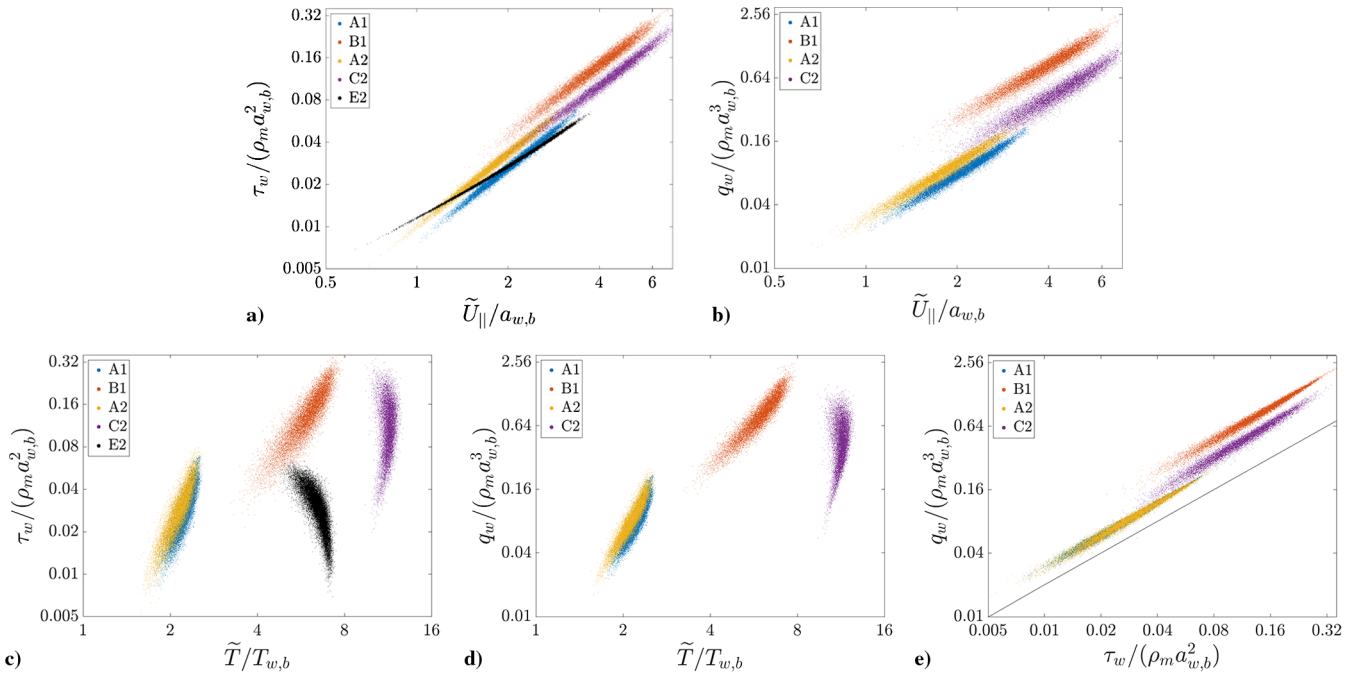

Fig. 8 Local and instantaneous top-wall values of a) shear stress, and b) heat flux from the wall model as functions of the local and instantaneous LES velocity at the matching location on a log–log scale. The frame of reference moves at the top-wall speed. Local top-wall values of c) shear stress, and d) heat flux as functions of the local LES temperature at the matching location on a log–log scale. Last, Fig. 8e shows the local top-wall values of the heat flux as a function of the shear stress, where the straight line indicates slope 1.

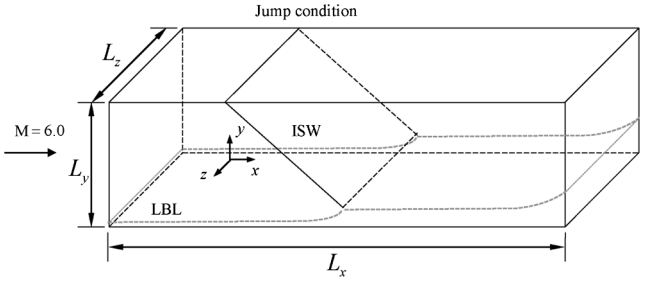

Fig. 9 Schematics of the computational set-up used for WMLES of a shock wave interacting with a transitional hypersonic boundary layer (ISW: incident shock wave; LBL: laminar boundary layer).

boundary layer height at the domain outlet, $\delta = 5.1\delta_o^*$, the grid resolution in the wall-parallel directions are $\Delta x = 0.23\delta$ and $\Delta z = 0.12\delta$ for WMLES1, and $\Delta x = 0.11\delta$ and $\Delta z = 0.061\delta$ for WMLES2. In the wall-normal direction, δ is resolved by 20 grid points in both simulations. The LES/wall-model matching location is $h_{\text{wm}} = 0.1\delta$. Such a resolution gives $\Delta x/h_{\text{wm}} \approx 2$ and $\Delta z/h_{\text{wm}} \approx 1$ for WMLES1 and $\Delta x/h_{\text{wm}} \approx 1$ and $\Delta z/h_{\text{wm}} \approx 0.5$ for WMLES2, which conforms to typical WMLES resolution [34]. Wall units at the streamwise location where the skin friction peaks are used for normalization here. Note that early DNS work in [35] on the same configuration employed a grid size of approximately 200 million cells. Those DNS results, along with experiments in two different facilities in the same configuration (RWG [36] and H2K [37]), are used later for comparisons.

The boundary conditions used in the WMLES are as follows. Periodicity is imposed in the spanwise direction, whereas a similarity solution for compressible laminar boundary layers is imposed at the inflow (see [38] for details). The inflow freestream Mach number is 6. The inflow displacement thickness of the boundary layer, the freestream speed of sound, the freestream density ρ_∞, and the freestream temperature T_∞ are taken as reference values to normalize lengths, velocities, densities, and temperatures. The resulting inflow Reynolds number is $Re_{\delta_o^\star} = 6830$ based on the inflow displacement thickness and on the freestream values of velocity, density, and viscosity, which corresponds to $Re_x = 0.3 \cdot 10^6$. In the present flow regime, where the deflection angle of the incident shock is not sufficiently large, the sole action of the shock is unable to cause transition, which would occur far away downstream from the impingement location. To trigger transition, the forcing method of [35] is followed, by which broadband acoustic disturbances are added to the inflow density as

$$\rho' = AW(y)\sum_{j=0}^{J}\cos(2\pi jz/L_z + \phi_j)\sum_{k=1}^{K}\sin(2\pi f_k t + \psi_k)$$

where ϕ_j and ψ_k are random phases, $f = 0.12$ is the base frequency, and $J = 16$ and $K = 20$ are cutoff wave numbers. Additionally, $W(y) = 1 - e^{-y^3}$ is a window function that dampens the disturbances within the boundary layer. The disturbance amplitude is $A = 0.001$ at the WMLES inlet, as opposed to $A = 0.0005$ in the DNS. Further comments about this necessary mismatch are provided later. Note that the DNS did not aim at exactly matching the disturbance level of the experiments, which are challenging to characterize, but demonstrated that the numerical results fall between the experimental heat transfer curves when appropriate levels are employed (see [35] and discussion later).

The wall temperature is kept constant and uniform at $T_w = 4.5T_\infty$. Rankine–Hugoniot jump conditions are used downstream from the shock to obtain the corresponding boundary values necessary for an obliquely impinging shock wave arising from an inviscid flow over the 4°-wedge used in the experiments. A characteristic Navier–Stokes boundary condition is superimposed on the top boundary to warrant nonreflectivity of pressure waves. The shock-impingement location computed from the inviscid wave propagation is at $x/\delta_o^\star = 150$, which translates into a local Reynolds number $Re_x = 1.34 \times 10^6$. A nonreflecting sponge layer of streamwise thickness $\Delta x = 10$ is placed near the outflow. The molecular viscosity in the equilibrium wall model and in the outer LES varies with temperature according to the Sutherland's law $\mu/\mu_{\text{ref}} = (T/T_{\text{ref}})^{1.5}[(T_{\text{ref}} + S)/(T + S)]$, where $S/T_{\text{ref}} = 1.69$ is a constant, and T_{ref} is set equal to the freestream temperature.

Instantaneous contours of the spanwise-averaged magnitude of the resolved density gradient from WMLES2 are shown in Fig. 10. The reflected flow structure consists of three different parts: 1) a compression shock emanating from upstream of the interaction zone,

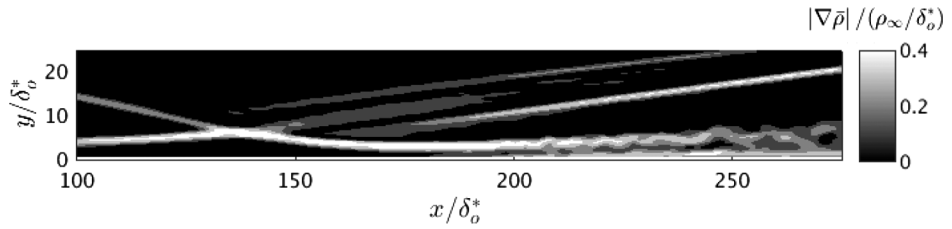

Fig. 10 Instantaneous isocontours of the spanwise-averaged magnitude of the resolved density gradient in case WMLES2.

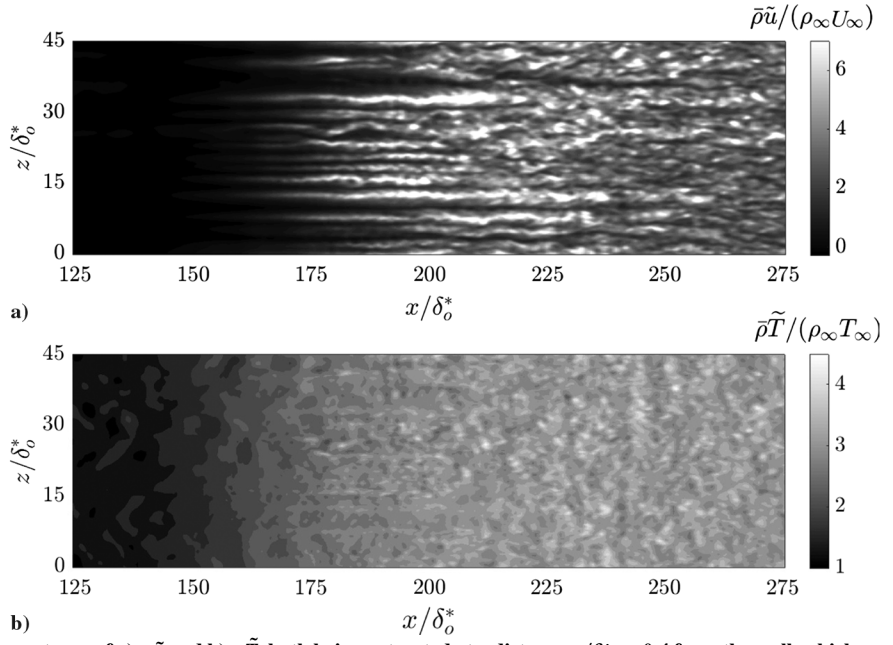

Fig. 11 Instantaneous isocontours of a) $\bar{\rho}\,\tilde{u}$ and b) $\bar{\rho}\,\tilde{T}$, both being extracted at a distance $y/\delta_o^* = 0.4$ from the wall, which corresponds to the third LES grid point away from the wall in case WMLES2.

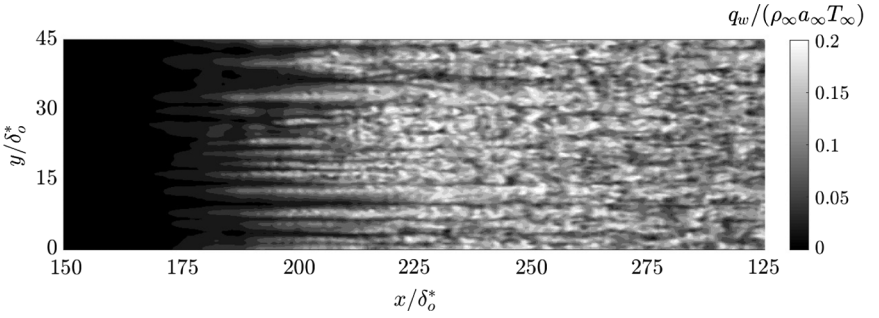

Fig. 12 Instantaneous isocontours of the wall heat-transfer flux predicted by the equilibrium wall model in case WMLES2.

which is generated by the upward flow deflection induced by the adverse pressure gradient created by the shock, 2) an expansion fan atop the interaction zone, and 3) a recompression shock downstream from the interaction zone created as the flow recovers its original direction. In addition, the shock-induced adverse pressure gradient produces a separation bubble that entrains cold freestream air and decreases the local effect of the aerodynamic heating.

The boundary layer rapidly undergoes transition downstream from the interaction region. The transition is clearly visible in the instantaneous streamwise momentum isocontours shown in Fig. 11a. Specifically, velocity streaks form that may be enhanced by Görtler-like instabilities engendered by the concave curvature of the streamlines along the edge of the boundary layer downstream of the interaction zone [39]. These transition dynamics are accompanied by a large increase in the near-wall flow temperature, as observed in Fig. 11b. Correspondingly, the dimensionless wall heat flux q_w shown in Fig. 12 undergoes a large increase upon transition. Remarkably, footprints of the velocity streaks are clearly discerned in the instantaneous wall heat transfer that highlight the importance of the near-wall momentum transport for heat-transfer modeling.

A more quantitative assessment of the wall heat-transfer rate is made in Fig. 13 in terms of the Stanton number

$$St = q_w/[\rho_\infty U_\infty c_p(T_r - T_w)] \tag{17}$$

where $T_r = T_\infty[1 + r(\gamma - 1)M_\infty^2/2]$ is the recovery temperature, and $r = Pr^{1/2} = 0.83$ is the recovery factor. In Eq. (17), the numerator is averaged in the spanwise direction and in time during eight flow-through times using eight snapshots. The resolved LES temperature is not significantly larger than the wall temperature anywhere in the LES grid. The near-wall peak in the static temperature, which is a result of the aerodynamic heating near the wall, is not resolved by the coarse LES grid but is modeled by the equilibrium wall model and leads to mostly grid-independent

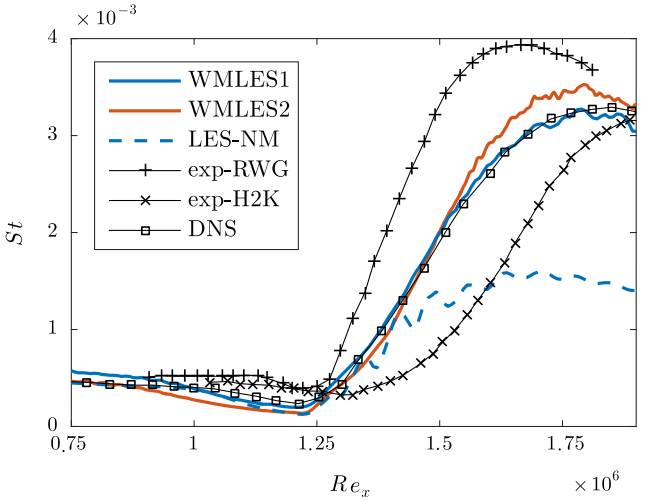

Fig. 13 Comparison of the Stanton numbers predicted by WMLES1 and WMLES2 using the equilibrium wall model, by experiments (RWG [37] and H2K [36]) and by DNS in [35]. LES with no wall model (LES-NM) is included for comparison.

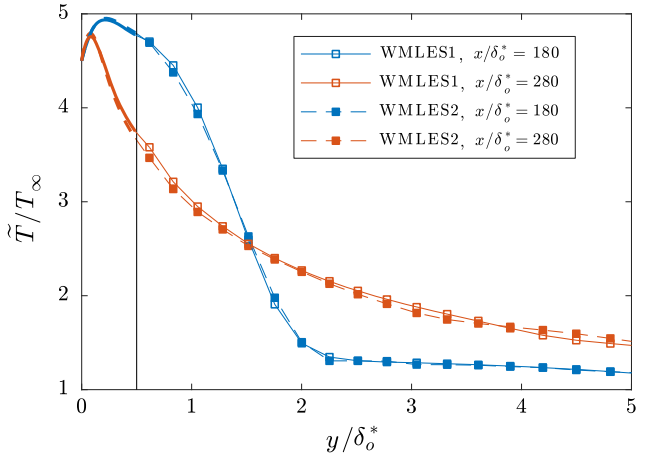

Fig. 14 Spanwise-averaged temperature profiles for WMLES1 and WMLES2 cases as a function of the wall normal distance at two streamwise locations downstream of the shock impingement. The vertical line represents the matching location with the wall model.

temperature profiles, as shown in Fig. 14. As a result, and for both grid resolutions tested here, the WMLES reproduces well the DNS results in [35]. This is in contrast to the results from LES with no wall model, which are performed on the same grid as WMLES1 and which largely underpredict the shock-induced heat transfer rates, as observed in Fig. 13. Note that WMLES2 predicts a slightly higher peak Stanton number than WMLES1, as expected by the increased spatial support for the growth of the inlet disturbances.

It is worth mentioning that the differences between the DNS and the experiments in Fig. 13 are due to discrepancies in the turbulence level within and above the boundary layer near the shock-impingement location. The DNS can match the experiments by adjusting the turbulence level at the inlet such that it matches that of the experiments. Because WMLES cannot capture the evolution of disturbance in the transitional region, for LES to match the experiments, the disturbances at the inlet must be adjusted such that turbulence levels similar to DNS are obtained near the impingement region. Further investigations are therefore needed to model the flow in the transitional region, particularly in regimes of low shock strengths when transition highly depends on the dynamics in the upstream laminar zone. These analyses may include extensions to high-speed flows of the treatment of the growth of the intrinsic boundary-layer instabilities in coarse grids as done, for instance, in [40] using disturbance models based on the parabolized Navier–Stokes equations. In conclusion, Fig. 13 shows that the equilibrium wall model provides a good prediction of the DNS results at a much lower computational cost, provided that the inflow turbulence level in WMLES is adjusted appropriately, as described previously.

V. Conclusions

In this work, the equilibrium wall model is investigated within the context of high-speed flows where convective aerodynamic heating becomes an important effect in quantifying wall heat-transfer rates. The formulation of the model is described with emphasis on heat-transfer aspects. Focus is made on two different configurations: high-speed turbulent Couette flows, and shock-wave interactions with transitional hypersonic boundary layers. Because the distance from the wall to the spatial location of the maximum of the aerodynamic-heating rate scales with inner viscous units, typical large-eddy simulations (LES) grids, whose resolution in the wall-normal direction scales with outer units, tend to miss the corresponding temperature peak. However, in coarse LES grids, the equilibrium wall model is able to account for subgrid-scale aerodynamic heating and provides predictions of wall heat-transfer rates that are indistinguishable from those in finer LES grids, in which the near-wall resolution is sufficient to resolve the aerodynamic heating.

In high-speed turbulent Couette flows, the wall model leads to predictions of wall heat-transfer rates that remain mostly grid-independent when different computations are performed in grids which are vastly different in size. Similarly, the model is able to reproduce the DNS wall heat-transfer rate in the problem of a shock impinging on a transitional supersonic boundary layer. Despite the presence of flow separation and a strong adverse pressure gradient, realistic predictions of the mean wall heat-transfer rate are found in the present wall-modeled large-eddy simulation (WMLES) calculation that uses merely 1 million cells as compared to the much more costly DNS. These considerations highlight the importance of correctly capturing the subgrid-scale aerodynamic heating in WMLES.

Enhanced predictions of higher-order statistics, particularly in situations where adverse pressure gradients play an important role, might require nonequilibrium wall-model effects to be included [33,41], but these are beyond the scope of this investigation. Note, however, that close to the wall the flow is subsonic, and the corresponding streamwise pressure gradients operate along much longer distances than close to the boundary-layer edge where the flow is supersonic and is impinged by the shock. Similarly, there are several other wall-modeling aspects that may influence the heat-transfer rates and remain largely unexplored in WMLES of high-speed aerothermodynamics, such as radiative aerodynamic heating, nonequilibrium gasdynamic effects in energy transfer, and near-wall chemical reactions, including ionization, ablation, and dissociation–recombination processes. It should, however, be mentioned that some of those tend to increase the temperature in the boundary layer and correspondingly decrease the characteristic Reynolds number. Further analyses of these additional effects within the context of WMLES are deferred to future work.

Acknowledgement

This work is funded by the U.S. Air Force Office of Scientific Research, grant 1194592-1-TAAHO.

References

[1] Urzay, J., "Supersonic Combustion in Air-Breathing Propulsion Systems for Hypersonic Flight," *Annual Review of Fluid Mechanics*, Vol. 50, 2018, pp. 593–627. doi:10.1146/annurev-fluid-122316-045217

[2] Hirschel, E., and Weiland, C., *Selected Aerothermodynamic Design Problems of Hypersonic Flight Vehicles*, Springer, Berlin, 2009.

[3] Durbin, P., "Toward Improved Prediction of Heat Transfer on Turbine Blades," *Journal of Turbomachinery*, Vol. 124, No. 2, 2002, pp. 187–192. doi:10.1115/1.1458020

[4] Annand, W., "Heat Transfer in the Cylinders of Reciprocating Internal Combustion Engines," *Proceedings of the Institution of Mechanical Engineers*, Vol. 177, No. 1, 1963, pp. 973–996.

[5] Yang, Y., Verzicco, R., and Lohse, D., "Scaling Laws and Flow Structures of Double Diffusive Convection in the Finger Regime," *Journal of Fluid Mechanics*, Vol. 802, Sept. 2016, pp. 667–689. doi:10.1017/jfm.2016.484

[6] Han, Z., and Reitz, R. D., "A Temperature Wall Function Formulation for Variable-Density Turbulent Flows with Application to Engine Convective Heat Transfer Modeling," *International Journal of Heat and Mass Transfer*, Vol. 40, No. 3, 1997, pp. 613–625. doi:10.1016/0017-9310(96)00117-2

[7] Rakopoulos, C., Kosmadakis, G., and Pariotis, E., "Critical Evaluation of Current Heat Transfer Models Used in CFD In-Cylinder Engine Simulations and Establishment of a Comprehensive Wall-Function Formulation," *Applied Energy*, Vol. 87, No. 5, 2010, pp. 1612–1630. doi:10.1016/j.apenergy.2009.09.029

[8] Choi, H., and Moin, P., "Grid-Point Requirements for Large Eddy Simulation: Chapman's Estimates Revisited," *Physics of Fluids*, Vol. 24, No. 1, 2012, Paper 011702. doi:10.1063/1.3676783

[9] Piomelli, U., and Balaras, E., "Wall-Layer Models for Large-Eddy Simulations," *Annual Review of Fluid Mechanics*, Vol. 34, No. 1, 2002, pp. 349–374. doi:10.1146/annurev.fluid.34.082901.144919

[10] Piomelli, U., "Wall-Layer Models for Large-Eddy Simulations," *Progress in Aerospace Sciences*, Vol. 44, No. 6, 2008, pp. 437–446. doi:10.1016/j.paerosci.2008.06.001

[11] Stevens, R. J., Wilczek, M., and Meneveau, C., "Large-Eddy Simulation Study of the Logarithmic Law for Second-and Higher-Order Moments in Turbulent Wall-Bounded Flow," *Journal of Fluid Mechanics*, Vol. 757, Oct. 2014, pp. 888–907. doi:10.1017/jfm.2014.510

[12] Park, G. I., and Moin, P., "Space-Time Characteristics of Wall-Pressure and Wall Shear-Stress Fluctuations in Wall-Modeled Large Eddy Simulation," *Physical Review Fluids*, Vol. 1, No. 2, 2016, Paper 024404. doi:10.1103/PhysRevFluids.1.024404

[13] Yang, X. I. A., "On the Mean Flow Behaviour in the Presence of Regional-Scale Surface Roughness Heterogeneity," *Boundary Layer Meteorology*, Vol. 161, No. 1, 2016, pp. 127–143.

[14] Jacob, C., and Anderson, W., "Conditionally Averaged Large-Scale Motions in the Neutral Atmospheric Boundary Layer: Insights for Aeolian Processes," *Boundary Layer Meteorology*, Vol. 162, No. 1, 2016, pp. 1–21.

[15] Bou-Zeid, E., Overney, J., Rogers, B. D., and Parlange, M. B., "The Effects of Building Representation and Clustering in Large-Eddy Simulations of Flows in Urban Canopies," *Boundary Layer Meteorology*, Vol. 132, No. 3, 2009, pp. 415–436. doi:10.1007/s10546-009-9410-6

[16] Yang, X. I., Sadique, J., Mittal, R., and Meneveau, C., "Exponential Roughness Layer and Analytical Model for Turbulent Boundary Layer Flow over Rectangular-Prism Roughness Elements," *Journal of Fluid Mechanics*, Vol. 789, Feb. 2016, pp. 127–165. doi:10.1017/jfm.2015.687

[17] Sayadi, T., and Moin, P., "Large Eddy Simulation of Controlled Transition to Turbulence," *Physics of Fluids*, Vol. 24, No. 11, 2012, Paper 114103. doi:10.1063/1.4767537

[18] Moeng, C. H., "A Large-Eddy-Simulation Model for the Study of Planetary Boundary-Layer Turbulence," *Journal of the Atmospheric Sciences*, Vol. 41, No. 13, 1984, pp. 2052–2062. doi:10.1175/1520-0469(1984)041<2052:ALESMF>2.0.CO;2

[19] Grötzbach, G., "Direct Numerical and Large Eddy Simulation of Turbulent Channel Flows," *Encyclopedia of Fluid Mechanics*, edited by N. P. Cheremisinoff, Gulf, West Orange, NJ, 1987, pp. 1337–1391.

[20] Bermejo-Moreno, I., Campo, L., Larsson, J., Bodart, J., Helmer, D., and Eaton, J. K., "Confinement Effects in Shock Wave/Turbulent Boundary Layer Interactions Through Wall-Modelled Large-Eddy Simulations," *Journal of Fluid Mechanics*, Vol. 758, Nov. 2014, pp. 5–62. doi:10.1017/jfm.2014.505

[21] Vane, Z., Bermejo-Moreno, I., and Lele, S. K., "Wall-Modeled Large-Eddy Simulations of a Supersonic Turbulent Flow in a Square Duct," *44th AIAA Fluid Dynamics Conference*, AIAA Paper 2014-2209, 2014.

[22] Larsson, J., Laurence, S., Bermejo-Moreno, I., Bodart, J., Karl, S., and Vicquelin, R., "Incipient Thermal Choking and Stable Shock-Train Formation in the Heat-Release Region of a Scramjet Combustor. Part 2: Large Eddy Simulations," *Combustion and Flame*, Vol. 162, No. 4, 2015, pp. 907–920. doi:10.1016/j.combustflame.2014.09.017

[23] Kawai, S., and Larsson, J., "Wall-Modeling in Large Eddy Simulation: Length Scales, Grid Resolution, and Accuracy," *Physics of Fluids*, Vol. 24, No. 1, 2012, Paper 015105. doi:10.1063/1.3678331

[24] Bradshaw, P., and Huang, G., "The Law of the Wall in Turbulent Flow," *Proceedings of the Royal Society of London A*, Vol. 451, No. 1941, 1995, pp. 165–188. doi:10.1098/rspa.1995.0122

[25] Kays, W., and Crawford, M., *Convective Heat and Mass Transfer*, McGraw–Hill, New York, 1993, pp. 258–272, Chap. 9.

[26] Khalighi, Y., Nichols, J. W., Lele, S., Ham, F., and Moin, P., "Unstructured Large Eddy Simulation for Prediction of Noise Issued from Turbulent Jets in Various Configurations," *17th AIAA/CEAS Aeroacoustics Conference*, AIAA Paper 2011-2886, June 2011.

[27] Joo, J., Medic, G., Philips, D., and Bose, S., "Large-Eddy Simulation of a Compressor Rotor," *Proceedings of the Summer Program*, Center for Turbulence Research, Stanford Univ., 2014, p. 467.

[28] Park, G. I., "Wall-Modeled Large-Eddy Simulation of a High Reynolds Number Separating and Reattaching Flow," *AIAA Journal*, Vol. 55, No. 11, 2017, pp. 3709–3721.

[29] You, D., and Moin, P., "A Dynamic Global-Coefficient Subgrid-Scale Eddy-Viscosity Model for Large-Eddy Simulation in Complex Geometries," *Physics of Fluids*, Vol. 19, No. 6, 2007, Paper 065110. doi:10.1063/1.2739419

[30] Moin, P., Squires, K., Cabot, W., and Lee, S., "A Dynamic Subgrid-Scale Model for Compressible Turbulence and Scalar Transport," *Physics of Fluids*, Vol. 3, No. 11, 1991, pp. 2746–2757. doi:10.1063/1.858164

[31] Ducros, F., Ferrand, V., Nicoud, F., Weber, C., Darracq, D., Gacherieu, C., and Poinsot, T., "Large-Eddy Simulation of the Shock/Turbulence Interaction," *Journal of Computational Physics*, Vol. 152, No. 2, 1999, pp. 517–549. doi:10.1006/jcph.1999.6238

[32] Bhagatwala, A., and Lele, S. K., "A Modified Artificial Viscosity Approach for Compressible Turbulence Simulations," *Journal of Computational Physics*, Vol. 228, No. 14, 2009, pp. 4965–4969. doi:10.1016/j.jcp.2009.04.009

[33] Park, G. I., and Moin, P., "An Improved Dynamic Non-Equilibrium Wall-Model for Large Eddy Simulation," *Physics of Fluids*, Vol. 26, No. 1, 2014, Paper 015108. doi:10.1063/1.4861069

[34] Larsson, J., Kawai, S., Bodart, J., and Bermejo-Moreno, I., "Large Eddy Simulation with Modeled Wall-Stress: Recent Progress and Future Directions," *Mechanical Engineering Reviews*, Vol. 3, No. 1, 2016, p. 15-00418.

[35] Sandham, N., Schülein, E., Wagner, A., Willems, S., and Steelant, J., "Transitional Shock-Wave/Boundary-Layer Interactions in Hypersonic Flow," *Journal of Fluid Mechanics*, Vol. 752, Aug. 2014, pp. 349–382. doi:10.1017/jfm.2014.333

[36] Willems, S., Gülhan, A., and Steelant, J., "Experiments on the Effect of Laminar–Turbulent Transition on the SWBLI in H2K at Mach 6," *Experiments in Fluids*, Vol. 56, No. 3, 2015, pp. 1–19. doi:10.1007/s00348-015-1904-z

[37] Schülein, E., "Effects of Laminar-Turbulent Transition on the Shock-Wave/Boundary-Layer Interaction," AIAA Paper 2014-3332, 2014.

[38] White, F. M., and Corfield, I., *Viscous Fluid Flow*, McGraw–Hill, New York, 2006, pp. 233–254, Chap. 4.

[39] Anubhav, D., Nichols, J., Jovanovic, M., and Candler, G., "Optimal Spatial Growth of Streaks in Oblique Shock/Boundary Layer Interaction," *8th AIAA Theoretical Fluid Mechanics Conference*, AIAA Paper 2017-4163, 2017.

[40] Lozano-Duran, A., Hack, M. J. P., Park, G. I., and Moin, P., "Modeling Boundary-Layer Transition in DNS and LES Using Parabolized Stability Equations," *Annual Research Briefs*, Center for Turbulence Research, Stanford Univ., 2016, pp. 29–37.

[41] Yang, X., Sadique, J., Mittal, R., and Meneveau, C., "Integral Wall Model for Large Eddy Simulations of Wall-Bounded Turbulent Flows," *Physics of Fluids*, Vol. 27, No. 2, 2015, Paper 025112.

J. P. Drummond
Associate Editor